J Adv Ceram

Research Article

# Intergrown columnar clusters toughening silicon nitride ceramics

Xiaowei Qin[1,2], Ji Zou[1], Weimin Wang[1], Wei Ji[1,2,✉], Zhengyi Fu[1,2,✉]

Cite this article: Qin X, Zou J, Wang W, et al. *J Adv Ceram* 2026, **15**(6): 9221303. https://doi.org/10.26599/JAC.2026.9221303

**ABSTRACT:** Silicon nitride ($Si_3N_4$) is an excellent candidate for engineering ceramics; however, its toughness and hardness remain fundamentally constrained by the inherent limitations arising from the incompatible α-phase (characterized by high hardness) and β-phase (characterized by high toughness). Herein, we report the exploration of advanced $Si_3N_4$ ceramics enabled by an intergrown cluster microstructure, which achieves a synergistic enhancement in both toughness (10.2±0.3 MPa·m$^{1/2}$) and Vickers hardness (20.1±0.3 GPa). These synergistic properties represent the state-of-the-art among $Si_3N_4$ ceramics fabricated via liquid-phase sintering reported to date. The formation of columnar clusters is driven by a high-pressure-induced coarsening process. The established metastable growth mechanism may open an avenue for fabricating new-generation $Si_3N_4$ ceramics with superb performance.

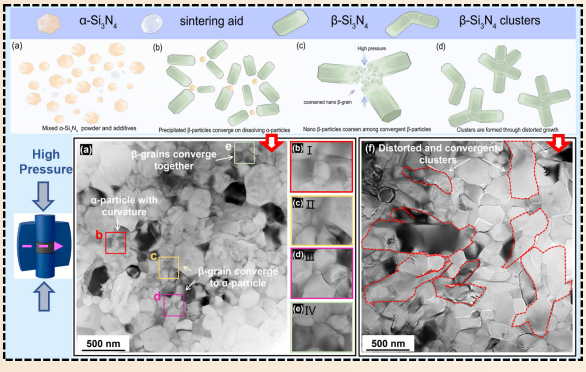


**KEYWORDS:** high-pressure sintering; silicon nitride; metastable growth; intergrown cluster; toughness

## 1 Introduction

Silicon nitride ($Si_3N_4$), a widely adopted engineering ceramic, demonstrates significant potential in emerging applications such as insulated gate bipolar transistor (IGBT) packaging, semiconductor substrates, and bioceramics due to its high theoretical thermal conductivity and excellent biocompatibility [1–3]. However, liquid-phase sintering, the dominant densification mechanism for $Si_3N_4$, restricts further performance enhancements [4]. The inherent phase transformation of this high-temperature process typically yields a β-phase-dominated microstructure. The precipitated β-phase grains exhibit anisotropic growth with high growth rates along certain crystallographic directions, leading to the formation of an interlocking microstructure that enhances strength and toughness [5–7]. Nevertheless, this high growth rate also tends to cause grain coarsening, making it difficult to precisely control microstructure evolution and thus limiting further improvements in properties [8].

High pressure lowers the required densification temperature below the phase transition point, thereby enabling the fabrication of dense, equiaxed α-phase $Si_3N_4$ ceramics characterized by high hardness but intrinsically low toughness [9]. Due to their distinct lattice stacking sequences, the α-phases and β-phases essentially represent high-hardness and high-toughness phases, respectively. The adjustments of processing parameters and powder composition to content allow the tuning of toughness and hardness by manipulating phase content [10], but they cannot overcome the performance bottleneck caused by the phase composition and grain morphology inherent to conventional sintering. Although novel silicon nitride architectures with a certain degree of compromise between toughness and hardness can be synthesized through complex processing or extreme high-pressure techniques, these high-cost approaches have yet to achieve a definitive breakthrough in the synergistic optimization of both properties [11–13].

Notably, a previous study on high-pressure-assisted liquid-phase sintering revealed that high pressure promoted phase transformation through a mechanism involving stress-induced interfacial migration [14,15]. This mechanism altering the microstructure by transcending the thermodynamic constraints of phase transformation avoided the performance limitations caused by microstructural and phase composition in conventional sintering. Consequently, a deeper investigation into the microstructural evolution and grain growth kinetics during metastable phase transitions under high-pressure stress can provide insights that break the limitations of traditional liquid-phase sintering, offering a theoretical basis and guidance for developing a new generation of high-performance $Si_3N_4$ ceramics. Based on previous experience with additive content and sintering

[1] State Key Laboratory of Advanced Technology for Materials Synthesis and Processing, Wuhan University of Technology, Wuhan 430070, China. [2] Hubei Longzhong Laboratory, Wuhan University of Technology Xiangyang Demonstration Zone, Xiangyang 441000, China.

✉ Corresponding authors. E-mail: W. Ji, jiwei@whut.edu.cn; Z. Fu, zyfu@whut.edu.cn

Received: February 10, 2026; Revised: April 18, 2026; Accepted: April 21, 2026

temperature, and to prevent grain coarsening and performance degradation induced by excessive liquid phase formation, samples were prepared using 2%, 4%, and 6% sintering aids and sintered at 1550 and 1600 °C for experimental investigation [14].

In this study, notably, at 1600 °C and 200 MPa, $Si_3N_4$ ceramics featuring a unique distorted morphology—with concurrent improvements in fracture toughness and hardness—were successfully fabricated. The results demonstrate that during liquid-phase sintering, the application of high pressure facilitates the distorted growth of precipitated grains by actively regulating interfacial stress.

## 2 Experimental

The starting raw materials included $Si_3N_4$ (α-phase content > 95%, oxygen content < 2 wt%, median particle size 0.2 μm, UBE), $Al_2O_3$ (purity > 99%, Macklin), and $Y_2O_3$ (purity > 99%, Macklin) with three different mixing ratios: 2 wt% ($Si_3N_4$ : $Al_2O_3$ : $Y_2O_3$ = 98 : 1 : 1), 4 wt% ($Si_3N_4$ : $Al_2O_3$ : $Y_2O_3$ = 96 : 2 : 2), and 6 wt% ($Si_3N_4$ : $Al_2O_3$ : $Y_2O_3$ = 94 : 3 : 3). The mixed powder was then dispersed in ethanol and planetary ball-milled for 8 h with $Si_3N_4$ balls. The resulting slurry was then dried, sieved through a 200-mesh sieve, and sintered via spark plasma sintering (SPS; ED-PAS-111, ELENIX, Japan) in a carbon fiber-reinforced die under 200 MPa.

The three different powder formulations were sintered at 200 MPa and temperatures of 1550 and 1600 °C. As a comparative sample, the powder containing 6 wt% additive was sintered under 50 MPa and 1700 °C. Sintering was conducted in a nitrogen atmosphere at 0.1 MPa, with a heating rate of 100 °C·min$^{-1}$. Each specimen was held at the peak temperature for 20 min. For high-pressure sintering at 200 MPa, an initial pressure of 50 MPa was applied, which was increased to 200 MPa before the temperature reached 600 °C.

Crystal structures were characterized with an X-ray diffractometer (XRD; Empyrean, PANalytical B.V., the Netherlands). The quantitative phase composition of all samples was determined by Rietveld refinement using Fullprof software. The resulting goodness-of-fit indicators were all below 15%, confirming the high reliability of the refinement results [16]. Microstructural analysis was performed on polished and plasma-etched surfaces with a scanning electron microscope (SEM; Regulus 8230, Hitachi Ltd., Japan). The $CF_4$ ion etching process required 50 W at 2 Pa for 5 min. Detailed microstructures were examined with a transmission electron microscope (TEM; Talos F200S, FEI, USA). The average grain size and average grain aspect ratio were statistically calculated with ImageJ software on ion-etched images, and at least 800 grains were analyzed. Vickers hardness was measured after a load of 19.6 N was applied for 15 s (Innovatest Europe B.V., the Netherlands). Fracture toughness was evaluated using the Vickers indentation method [17]. A VHX-7000 digital microscope (Keyence) was used to take images of the fracture surfaces of the samples. Given the small dimensions of the specimens sintered under high pressure, which prevented direct elastic modulus ($E$) measurement, a standard value of 300 GPa, typical for conventional $Si_3N_4$, was used in calculations. A constraint factor of 3 was applied in the analytical model. The bulk density of the sintered specimens was determined via the Archimedes method.

The biaxial flexural strength was measured on sintered disc samples with a diameter of 15 mm and a thickness of 1 mm. The hardness, toughness, and flexural strength values of each sample were determined by averaging the results obtained at seven indentations. Samples were designated according to temperature–pressure and additive content (e.g., 1550–200-2 denotes 1550 °C and 200 MPa with 2 wt% additives).

## 3 Results and discussion

XRD analysis of the samples sintered under 200 MPa revealed that the liquid phase content is the critical factor governing the phase transformation of $Si_3N_4$. With the addition of a 2 wt% sintering aid, negligible phase transformation occurred at 1550 °C, and the α-phase content was measured as 96.15% (Table 1). The bulk densities of the samples, measured by the water displacement method, indicated that near-full densification was achieved in most cases (Table 2), with only the 1550–200-2 sample exhibiting a slightly lower relative density. In the case of the 1600–200-2 sample, raising the temperature by 50 °C only resulted in a slight decrease in the α-phase content from 96.16% to 93.43%. The microstructure of the 1600–200-2 sample (Fig. 1(e)) was primarily composed of equiaxed grains, with numerous large particles exhibiting features of dynamic grain growth, such as cluster-like aggregation and intragranular pores [18]. Additionally, needle-like grains, identified as precipitated β-phase particles, were occasionally observed within sparse white liquid phase regions (indicated by red arrows). These findings suggest that in the absence of a sufficient liquid phase, densification is predominantly driven by quasiplastic deformation mediated by particle rearrangement and sliding—even at temperatures above the phase transformation threshold.

**Table 1** Analyzed phase content of all sintered samples (Unit: %)

| Sample | α-phase | β-phase |
|---|---|---|
| 1550–200-2 | 96.15 | 3.85 |
| 1550–200-4 | 58.35 | 41.64 |
| 1550–200-6 | 42.05 | 57.95 |
| 1600–200-2 | 93.43 | 6.57 |
| 1600–200-4 | 52.75 | 47.25 |
| 1600–200-6 | 18.91 | 81.09 |
| 1700–50-6 | 20.20 | 79.80 |

**Table 2** Characteristics and performance parameters of all sintered samples

| Sample | Raletive dentisy (%) | Average grain size (μm) | Average grain aspect ratio | Vickers hardness (GPa) | Facture toughness (MPa·m$^{1/2}$) | Biaxial flexural strength (MPa) |
|---|---|---|---|---|---|---|
| 1550–200-2 | 97.8 | 0.21 | 1.10 | 23.7±0.3 | 3.5±0.2 | 293±25 |
| 1550–200-4 | 98.8 | 0.29 | 1.11 | 22.4±0.4 | 4.5±0.2 | 583±67 |
| 1550–200-6 | 99.3 | 0.31 | 1.41 | 21.9±0.3 | 5.8±0.3 | 600±59 |
| 1600–200-2 | 98.6 | 0.29 | 1.12 | 22.9±0.3 | 3.8±0.3 | 367±29 |
| 1600–200-4 | 99.2 | 0.40 | 1.47 | 20.9±0.2 | 6.1±0.2 | 726±57 |
| 1600–200-6 | 99.3 | 0.47 | 1.65 | 20.1±0.3 | 10.2±0.3 | 982±63 |
| 1700–50-6 | 98.2 | 0.32 | 1.46 | 18.4±0.3 | 6.8±0.3 | 936±52 |

When the additive content was increased to 4 and 6 wt%, the phase transformation behavior varied significantly depending on both the liquid phase volume and temperature. With 4 wt% additive, the β-phase content formed after sintering at 1550 °C was 41.64%, which increased to 47.25% when the temperature was raised by 50 °C. With 6 wt% additive samples, the phase transformation was already more than 50% complete at 1550 °C, with a β-phase content of 57.95%. At the higher temperature of 1600 °C, the transformed phase content reached 81.09%. The microstructural evolution observed in the SEM images of the 4 and 6 wt% samples (Figs. 1(d) and 1(c)) was consistent with the phase transformation trends indicated by XRD analysis (Fig. 1(a)). At 1600 °C, both samples developed columnar grains characterized by intergrown and distorted morphologies, as marked by red dashed lines. This microstructural trend was particularly pronounced in the 6 wt% sample.

Conversely, although the sample sintered at 1700 °C under 50 MPa (low pressure and high temperature) achieved a β-phase content of 79.80%, comparable to that of the 1600 °C–200 MPa (6 wt% additive) sample, its microstructure differed significantly. The ion-etched SEM image (Fig. 1(b)) reveals a matrix composed of elongated columnar grains and a white liquid phase embedded with numerous fine particles. According to XRD results indicating 79.80% β-phase content, these fine particles, which are smaller than the initial powder size of 200 nm, are identified as newly formed β-phase nuclei, in particular nanoparticles with irregular morphology. The slightly larger equiaxed grains observed around the white liquid phase are likely undissolved α-phase particles.

In short, distorted clusters in the 1600–200-6 sample were formed because high pressure enhanced the growth of grains precipitated from the liquid phase. Table 2 shows the Vickers hardness, biaxial flexural strength, and fracture toughness of all samples. The mechanical properties were closely correlated with the phase composition. The 1550–200-2 sample exhibited a high hardness of 23.7 GPa, low fracture toughness (3.5 MPa·m$^{1/2}$), and low flexural strength (293 MPa). When the additive content increased to 4 and 6 wt%, along with the increasing extent of phase transformation, the hardness of the samples decreased, whereas both the strength and toughness increased. This trend was more pronounced in the samples sintered at 1600 °C.

Notably, the 1600–200-6 sample exhibited distorted grain growth and a hardness of 20.1±0.3 GPa, but it unexpectedly attained superior toughness (10.2±0.3 MPa·m$^{1/2}$) and strength (982±63 MPa). In contrast, the 1700–50-6 sample characterized by interlocking columnar grains demonstrated a flexural strength of 936±52 MPa and toughness of 6.8±0.3 MPa·m$^{1/2}$. However, due to the fine and uniform grain size and the presence of residual equiaxed α-$Si_3N_4$ particles that did not undergo phase transformation, the hardness remained at a level of 18.4±0.3 GPa.

Figure 2(a) illustrates the relationship between the Vickers hardness and fracture toughness for the samples synthesized in this work and $Si_3N_4$ ceramics in previous studies. Mainstream commercial $Si_3N_4$ mainly composed of the β-phase typically displays a performance envelope defined by a fracture toughness of 4–8 MPa·m$^{1/2}$ and a hardness of 14 to 18 GPa, which primarily depend on the grain size and aspect ratio of β-grains. Various strategies (Fig. 2(a)), such as process optimization, multistep sintering, and fiber reinforcement, successfully enhanced individual properties, but they did not resolve the inherent trade-off between hardness and toughness caused by the phase content. Remarkably, the 1600–200-6 sample developed in this study overcame these limitations, increased fracture toughness and maintained high hardness. This result suggested a significant breakthrough relative to the conventional performance limits of liquid-phase sintered $Si_3N_4$.

Figures 2(b)–2(e) illustrate the typical indentation crack propagation morphologies of silicon nitride ceramics fabricated under various processing parameters, revealing the decisive influence of microstructural anisotropy on fracture resistance. In the 1600–200-2 specimen, the crack path is remarkably straight with the maximum extension length, primarily attributed to a microstructure dominated by equiaxed grains. Due to the lack of effective spatial hindrance, the crack propagates via a low-energy-dissipative intergranular fracture mode, reflecting the characteristic failure of inherently brittle materials. Conversely, with increasing sintering temperature or additive content, the substantial development of elongated columnar grains triggers a pronounced crack deflection mechanism. As shown in Figs. 2(c) and 2(d), these high-aspect-ratio grains force the crack tip to deviate continuously from its original trajectory, resulting in a highly tortuous path that significantly increases the cumulative fracture surface area and dissipates substantial elastic energy.

Comparative observations indicate that the fracture resistance of 1700–50-6 is slightly superior to that of 1600–200-4. Although both exhibit enhanced toughness, 1700–50-6 benefits from a higher β-phase content and a dense population of fine elongated columnar grains, which effectively absorb crack energy through extensive transgranular fracture. In contrast, the crack in

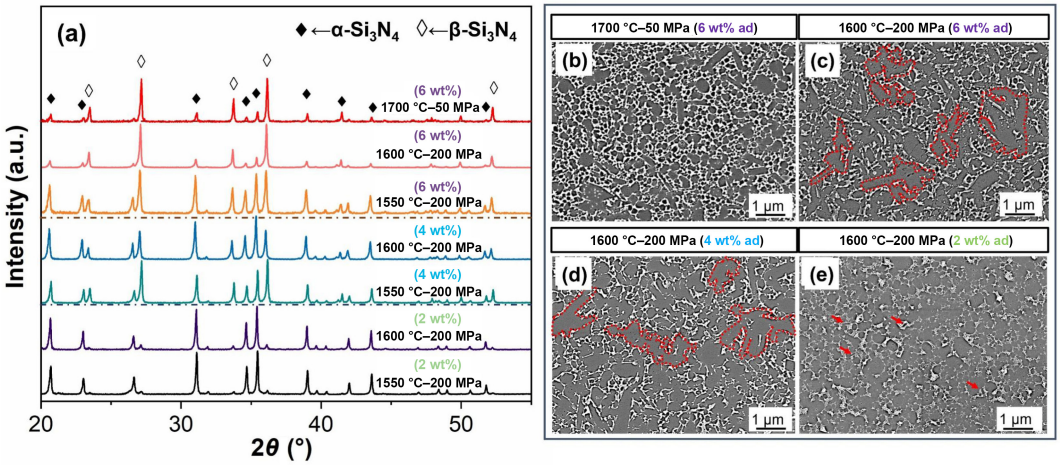


**Fig. 1** (a) XRD patterns of the sintered samples. (b–e) Ion-etched microstructures of the samples sintered under different conditions: (b) 1700 °C and 50 MPa (6 wt% additives), (c) 1600 °C and 200 MPa (6 wt% additives), (d) 1600 °C and 200 MPa (4 wt% additives), and (e) 1600 °C and 200 MPa (2 wt% additives).

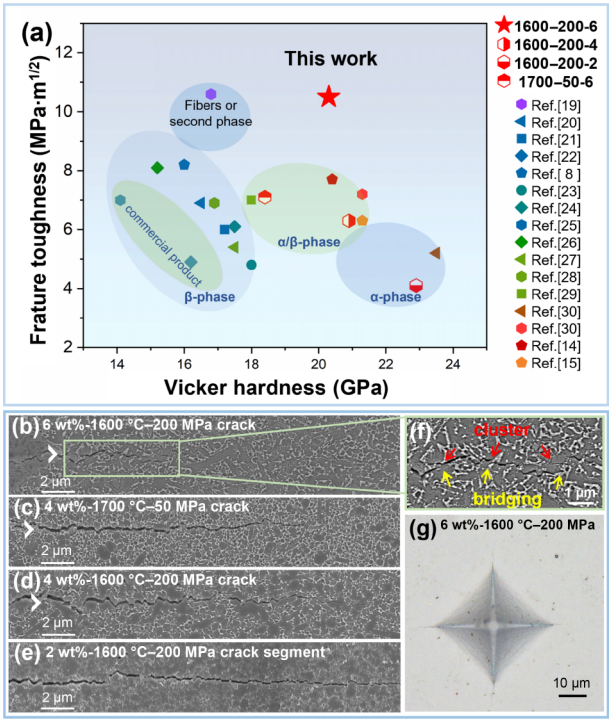


**Fig. 2** Mechanical properties and crack propagation behavior of the high-temperature sintered samples: (a) comparison of Vickers hardness and fracture toughness between the four high-pressure sintered samples and the data from relevant studies; (b–e) indentation crack propagation morphologies of samples: (b) 1600–200-6, (c) 1700–50-6, (d) 1600–200-4, and (e) 1600–200-2; (f) magnified view of the crack shown in (b). (g) Indentation micrograph of the 1600–200-6 sample.

1600–200-4 (Fig. 2(d)) is accompanied by evident intergranular fracture, transgranular fracture of large grains, and crack bridging, where the synergistic effect of cluster fracture and bridging inhibits crack expansion.

The 1600–200-6 sample exhibited optimal fracture toughness. It is uncommon to observe such high hardness combined with relatively short crack lengths, as evidenced by the indentation image in Fig. 2(g). A typical microstructural feature observed in Fig. 2(b) is the presence of distinct columnar grain clusters. These clusters manifest as coarse grain nodes exhibiting distinct internal stress–field distortion features. A magnified view of the crack segment from Fig. 2(b) (presented in Fig. 2(f)) reveals that the bridging grains (indicated by yellow arrows) are exclusively composed of columnar clusters (marked by red arrows). The bridges formed by fracture within these columnar clusters exert a substantial closure stress to counteract the crack-opening displacement [31]. Furthermore, the detachment of these distorted columnar grain clusters from the matrix (via intergranular fracture) necessitates immense frictional pull-out energy. Consequently, these distorted clusters effectively suppress crack propagation through a potent synergy between crack growth retardation and bridging mechanisms.

To elucidate the cluster formation mechanism in the 1600–200-6 sample, TEM analysis was performed on the microstructures of 6 wt% samples sintered at 1550 and 1600 °C. The morphological evolution indicated the profound influence of high pressure on the growth behavior of precipitated particles. The microstructure of the 1550–200-6 sample (Fig. 3(a)) exhibited a mixed morphology of equiaxed and columnar grains. The coexistence of columnar grains and large equiaxed particles characterized by intragranular pores and agglomerated features suggested that two distinct mechanisms existed in the late stage of densification: dynamic growth and phase transformation-induced growth [15,18]. Additionally, a small fraction of spherical particles with high-curvature interfaces were observed. In conventional sintering, grain interfaces typically become planar because the interface curvature serves as the primary driving force for grain boundary migration. However, under high-pressure densification, intense localized stress often leads to the formation of irregular or distorted interfaces. Therefore, the retention of these high-curvature particles during high-pressure liquid-phase sintering indicated the presence of incompletely dissolved α-phase particles. A clear correlation between the growth of columnar grains and these spherical particles existed. The growth of columnar grains exhibited a tendency to converge toward spherical particles. This convergent behavior was likely driven by the localized supersaturation in the liquid phase generated by the rapid dissolution of α-phase particles [5,6]. Roman numerals I to IV are labeled in the four insets of Figs. 3(b)–3(e) to illustrate the sequential process of grain convergence. Figure 3(b) shows multiple columnar grains encapsulating a spherical particle. Figures 3(c) and 3(d) depict adjacent columnar grains converging around a gradually dissolving α-phase particle. Figure 3(e) captures the state where neighboring columnar grains have fully converged. The TEM image of the 1600–200-6 sample (Fig. 3(f)) reveals significant microstructural transformations resulting from

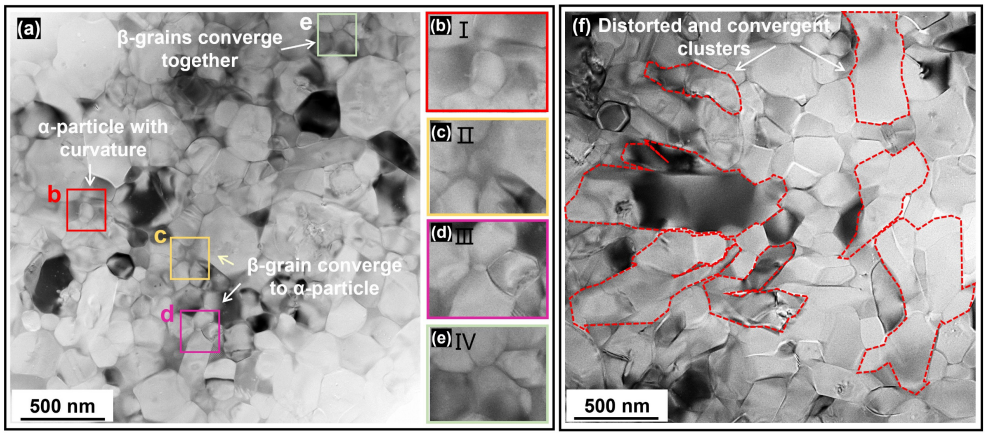


**Fig. 3** TEM micrographs of the samples sintered with 6 wt% additives: (a) general morphology of the 1550–200-6 sample; (b–e) high-resolution images of specific features: (b) columnar grains encapsulating a spherical α-phase particle, (c, d) adjacent columnar grains converging around dissolving α-phase particles, and (e) fully converged columnar grains; (f) microstructure of the 1600–200-6 sample with distorted columnar clusters.

the temperature increase of 50 °C. The α-phase particles were almost entirely absent, indicating a more complete dissolution–precipitation process. The grains evolved into larger, distorted, and intergrown columnar clusters (outlined by red dashed lines). When the complete dissolution of α-particles enhanced the clustering tendency of β-grains, the stress interaction between adjacent grains under high-pressure conditions during the late stage of densification also promoted the formation of these distorted growth morphologies.

Figure 4 presents TEM images and GPA analysis of the intergrown clusters in the 1600–200-6 sample. Figure 4(a) provides an overview of the general cluster morphology, where a remnant α-phase particle (tens of nanometers in size) was identified in boxes in Area b. The corresponding high-resolution TEM (HRTEM) image (Fig. 4(b)) highlights a significantly distorted boundary between this α-nanoparticle and the adjacent grains. Based on the inverse Fourier transform (IFT) patterns shown in the top-right insets of Figs. 4(c)–4(f), it is observed that these intersecting grains maintain highly consistent crystallographic orientations. Specifically, as illustrated in Fig. 4(c), although the two adjacent grains situated above the α-phase particle exhibit a tendency toward a unified lattice orientation, a misorientation angle of ~4° is observed between their respective undistorted lattice regions. Interestingly, the lattice mismatch between these two grains manifests as a continuous distorted zone devoid of a distinct, sharp interface. Furthermore, focusing on the boundary region at the contact area between the α-phase particle and adjacent grains (marked by the square in Fig. 4(b)), the HRTEM images and IFT patterns in Figs. 4(d)–4(f) reveal that the residual α-phase and the adjacent large β-phase grain share the same crystallographic orientation, forming a coherent heterophase interface. Undoubtedly, these distortions are induced by high-pressure stress. It is noteworthy, however, that such distortions manifest not only within the kinked β-columnar grains (Fig. 4(b)) but also at the phase boundaries of the α-phase, which is mechanically harder at lower temperatures. The preferential occurrence of these distortions on the α-side of the coherent interface likely stems from the lattice instability of the α-phase on the threshold of its phase transformation at elevated temperatures.

Regarding quasiboundaries with identical crystallographic orientations, Shen *et al.* [5] proposed that such quasiboundary morphology emerges during the ordered convergence of nano β-phase particles in the phase transformation process. This morphology represents a metastable "quasiboundary" state during particle convergence prior to the formation of larger grains. Unlike the quasiboundaries formed under low-pressure rapid

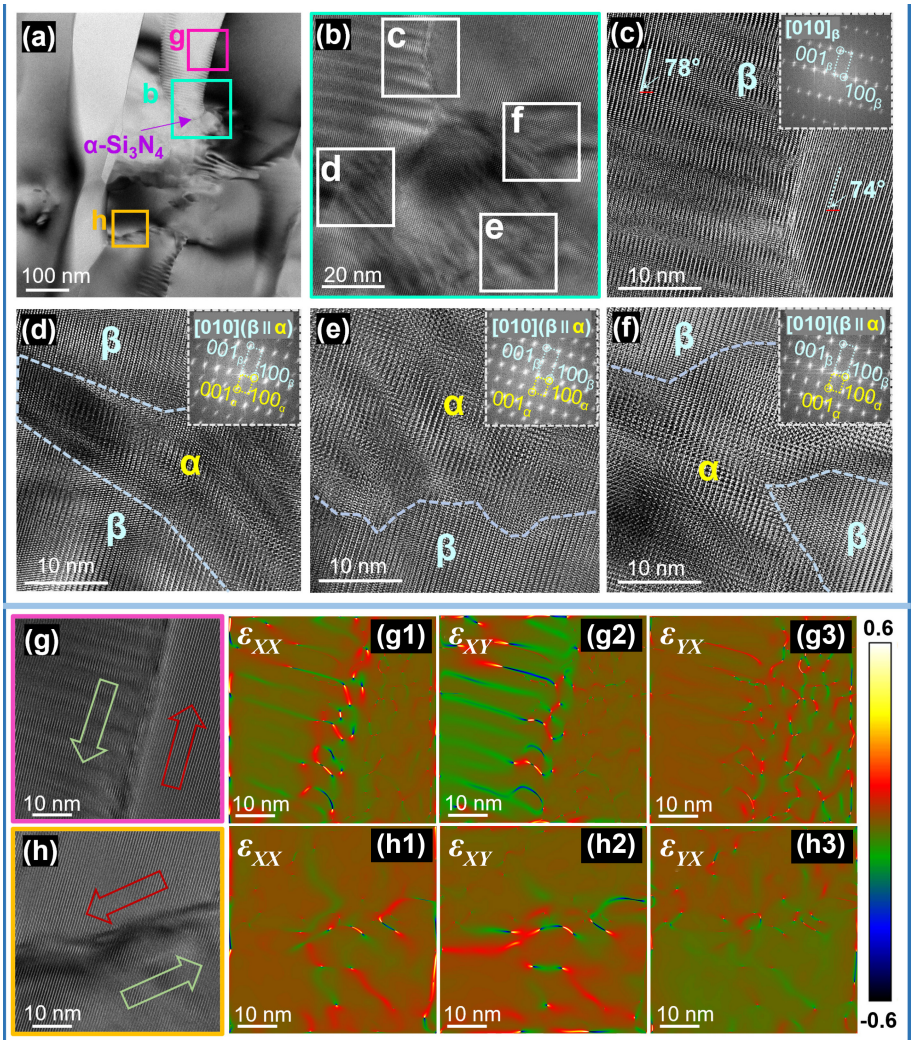


**Fig. 4** Microstructural analysis of the distorted columnar cluster of the 1600–200-6 sample: (a) general TEM morphology; (b) HRTEM image showing lattice distortion at the junction of three grains; (c–f) enlarged HRTEM images corresponding to the distorted regions marked in (b); (g, h) HRTEM images of the boundary regions marked by red and white boxes in (a), (g1–g3) and (h1–h3) corresponding GPA strain maps ($\varepsilon_{XX}$, $\varepsilon_{XY}$, and $\varepsilon_{YX}$) in (g, h).

sintering conditions reported by Shen, those observed in Fig. 4(a) exhibit significant lattice distortion. This strained "boundary" morphology likely results from stress-induced interfacial deformation during particle convergence under high pressure. The wrinkled "boundary" between two adjacent β-phase particles with identical orientations in Fig. 4(c), along with similar compressive wrinkling observed in the α-phase particle in Figs. 4(d)–4(f) suggests that high-pressure stress during β-phase particle convergence involves dynamic processes such as interfacial sliding and shear.

Geometric phase analysis (GPA) was performed on the grain interfaces highlighted in Regions g and h in Fig. 4(a), and pronounced wrinkling was observed. The corresponding HRTEM micrographs (Figs. 4(g) and 4(h)) revealed distinct signatures of interfacial sliding at the terminals of these wrinkled interfaces. In the corresponding GPA strain maps, significant stress–strain concentrations (indicated by the most pronounced color contrasts) were observed across the interfaces along the $\varepsilon_{XY}$ direction in Fig. 4(g2) and the $\varepsilon_{YX}$ direction in Fig. 4(h3). Moreover, the shear strain along the $\varepsilon_{XY}$ direction in Fig. 4(g) and the $\varepsilon_{YX}$ direction in Fig. 4(h) was parallel to the respective interfaces, indicating the presence of significant shear stress at the wrinkled interfaces and the occurrence of dynamic processes such as squeezing and shearing between adjacent grains.

Furthermore, a detailed investigation was conducted on the wrinkled region situated beneath the α-particle distorted zone in Fig. 4(a), with the corresponding TEM morphology presented in Fig. 5(a). High-magnification TEM imaging of the boxed region (b) in Fig. 5(a) (displayed in Fig. 5(b)) reveals a morphology resembling a distorted triangular grain boundary junction, resulting from the mutual squeezing and impingement of two large columnar grains against a central grain. The interfacial morphologies at the center (Fig. 5(c)) and the peripheral regions (Figs. 5(d) and 5(e)) were further characterized via HRTEM. Consistent crystallographic orientations across the entire distorted zone are confirmed by the diffraction patterns in Figs. 5(c)–5(e). The HRTEM images reveal a distinct directional preference in lattice distortion, as highlighted by the oval frames. Specifically, within the central region (Fig. 5(c)), the distortion manifests as numerous lattice misorientations aligned parallel to the (100) planes—essentially perpendicular to the *c*-axis direction. In the peripheral regions (Figs. 5(d) and 5(e)), the directional alignment of these lattice misorientations is found to be highly consistent with the contour of the quasiboundary profiles observed in Fig. 5(b). These findings demonstrate that during ordered coalescence along the *c*-axis, the converging particles undergo significant stress-induced squeezing and interfacial shearing, which fundamentally governs the evolution of the columnar grain cluster microstructure.

To illustrate the mechanism of cluster formation, a schematic diagram (Fig. 6) outlines the key evolutionary stages. Figure 6(a) shows the initial powder mixture of α-$Si_3N_4$ and sintering additives. Figure 6(b) illustrates the early stage of liquid-phase dissolution and phase transformation. Columnar grains under high pressure demonstrated a distinct convergent growth tendency. This phenomenon was driven by the high supersaturation of the liquid phase resulting from the rapid dissolution of metastable α-$Si_3N_4$. In the final stage of dissolution–precipitation (Fig. 6(c)), as the α-phase was nearly exhausted, adjacent columnar grains coalesced and grew. Driven by high compressive stress, these grains underwent mutual extrusion and sliding, ultimately resulting in distorted columnar grain clusters (Fig. 6(d)).

## 4 Conclusions

In conclusion, the effects of high pressure above the phase transformation temperature on phase transformation and grain growth during the final stage of densification were investigated under three different contents of sintering additives. It was found that the microstructure evolution and mechanical properties of $Si_3N_4$ sintered under a pressure of 200 MPa were highly dependent on the liquid phase content. A low additive content (2 wt%) yielded high-hardness α-$Si_3N_4$, and increasing the liquid

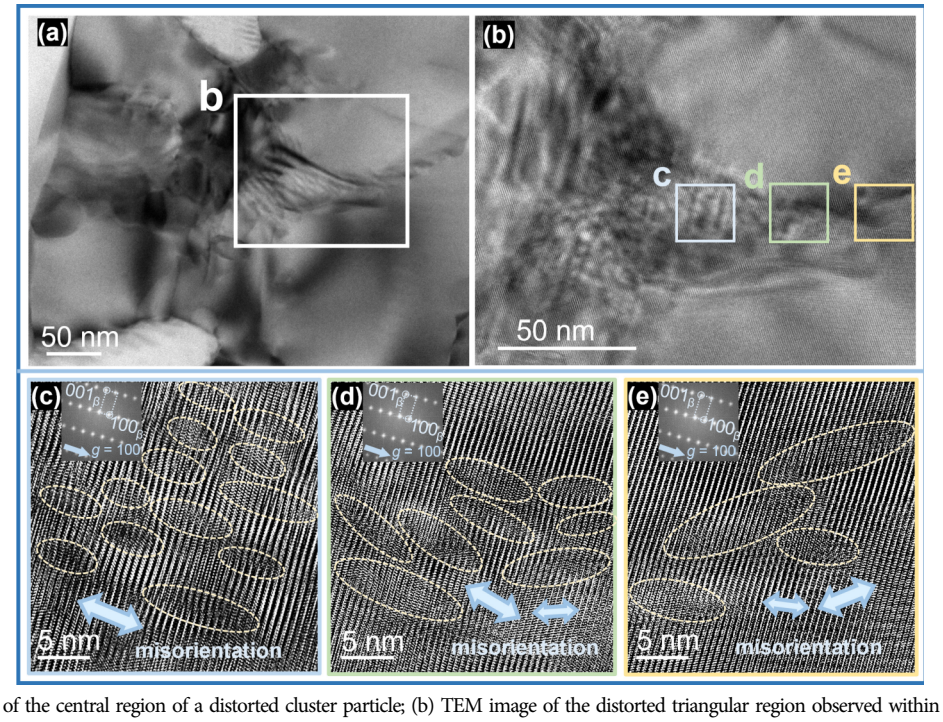


**Fig. 5** (a) TEM image of the central region of a distorted cluster particle; (b) TEM image of the distorted triangular region observed within the coarse grain in (a); (c–e) HRTEM images of the center and edge of the distorted region in (b).

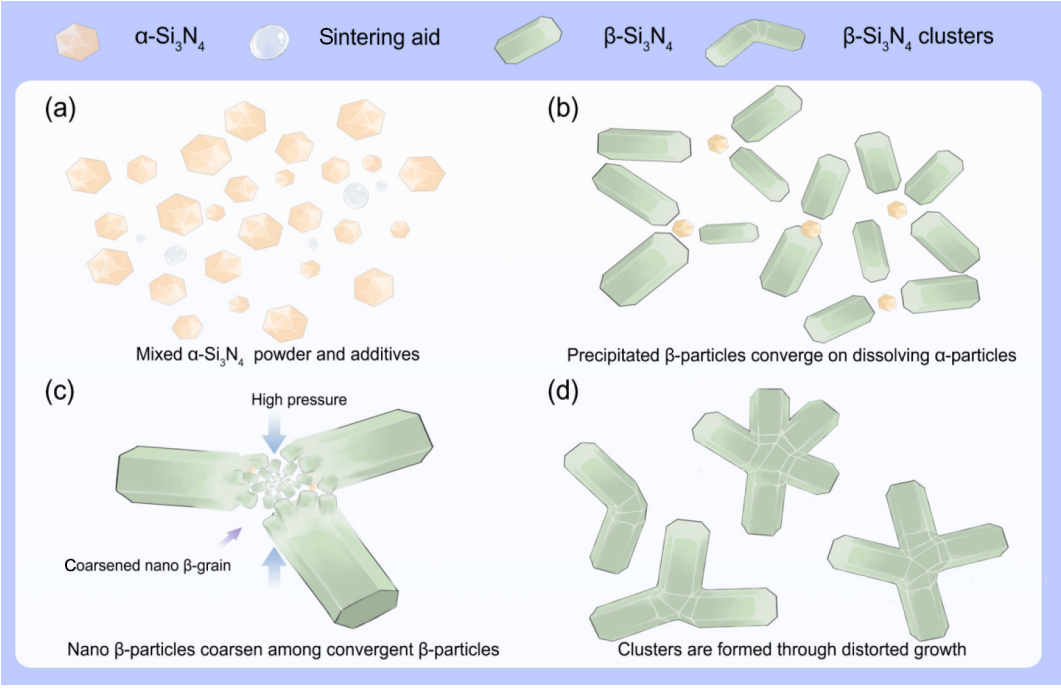


**Fig. 6** Mechanism of cluster formation: (a) initial powder mixture of α-$Si_3N_4$ and sintering additives, (b) convergent growth of β-grains toward the supersaturated regions of the liquid phase generated by the dissolution of α-particles, (c) coalescence of nanoparticles onto adjacent grains and subsequent distorted growth under stress, and (d) distorted columnar grain cluster.

phase to 4–6 wt% facilitated complete phase transformation, thus resulting in high strength and toughness. Notably, the 6 wt% sample sintered at 1600 °C achieved the simultaneous enhancement of strength (982±63 MPa), toughness (10.2± 0.3 MPa·$m^{1/2}$), and hardness (20.1±0.3 GPa). This improvement in performance is attributed to a unique twisted intergrowth mechanism, which involves stress-induced compression and shear during the ordered coalescence of precipitated particles in the phase transformation.

## Acknowledgements

This work was financially supported by the National Natural Science Foundation of China (Grant Nos. 52322207, 92163208, and 52494933), the Fundamental and Interdisciplinary Disciplines Breakthrough Plan of the Ministry of Education of China (No. JYB2025XDXM408), the Natural Science Foundation of Hubei Province (Nos. 2025AFA043 and 2025CSA004), and the Independent Innovation Projects of the Hubei Longzhong Laboratory (No. 2022ZZ–11).

## Availability of data and materials

The data that support the findings of this study are available from the corresponding author upon reasonable request.

## Competing interests

The authors have no competing interests to declare that are relevant to the content of this article.

## References

[1] Riley FL. Silicon nitride and related materials. *J Am Ceram Soc* 2000, **83**: 245–265.
[2] Krstic Z, Krstic VD. Silicon nitride: The engineering material of the future. *J Mater Sci* 2012, **47**: 535–552.
[3] Zhou Y, Hyuga H, Kusano D, *et al.* Development of high-thermal-conductivity silicon nitride ceramics. *J Asian Ceram Soc* 2015, **3**: 221–229.
[4] Lange H, Wötting G, Winter G. Silicon nitride—From powder synthesis to ceramic materials. *Angew Chem Int Ed* 1991, **30**: 1579–1597.
[5] Shen ZJ, Zhao Z, Peng H, *et al.* Formation of tough interlocking microstructures in silicon nitride ceramics by dynamic ripening. *Nature* 2002, **417**: 266–269.
[6] Hu JF, Shen ZJ. Ordered coalescence of nanocrystallites contributing to the rapid anisotropic grain growth in silicon nitride ceramics. *Scripta Mater* 2013, **69**: 270–273.
[7] Qin XW, Li S, Zhao L, *et al.* Silicon nitride ceramics consolidated by oscillatory pressure sintering. *Ceram Int* 2020, **46**: 14235–14240.
[8] Zhao S, Du SM, Zhang SJ, *et al.* Low-temperature rapid sintering for the fabrication of biphasic $Si_3N_4$ ceramics with outstanding mechanical properties. *J Adv Ceram* 2025, **14**: 9221044.
[9] Lukianova OA, Novikov VY, Parkhomenko AA, *et al.* Microstructure of spark plasma-sintered silicon nitride ceramics. *Nanoscale Res Lett* 2017, **12**: 293.
[10] Tang SJ, Guo WM, Sun SK, *et al.* Design strategy of phase and microstructure of $Si_3N_4$ ceramics with simultaneously high hardness and toughness. *J Adv Ceram* 2023, **12**: 122–131.
[11] Chen IW, Rosenflanz A. A tough SiAlON ceramic based on α-$Si_3N_4$ with a whisker-like microstructure. *Nature* 1997, **389**: 701–704.
[12] Li W, Yu ZJ, Wiehl L, *et al.* Hard and tough novel high-pressure γ-$Si_3N_4$/$Hf_3N_4$ ceramic nanocomposites. *J Adv Ceram* 2023, **12**: 1418–1429.
[13] Hou ZQ, Wang HK, Yang YN, *et al.* High-pressure synthesis of high-performance submicron-sized polycrystalline β-$Si_3N_4$ bulk without additives. *Ceram Int* 2020, **46**: 12449–12457.
[14] Liu SC, Pan Y, Feng BT, *et al.* Toughening of silicon nitride ceramics through stress-induced phase transformation. *J Adv Ceram* 2025, **14**: 9221125.
[15] Qin XW, Zou J, Wang WM, *et al.* High-pressure regulated phase transition enables *in situ* synthesis of high-performance dual-phase $Si_3N_4$ ceramics. *Sci China Mater* 2025, **68**: 4285–4291.
[16] Arcelus O, Rodríguez-Carvajal J, Katcho NA, *et al.* FullProfAPP: A graphical user interface for the streamlined automation of powder diffraction data analysis. *J Appl Crystallogr* 2024, **57**: 1676–1690.
[17] Niihara K, Morena R, Hasselman DPH. Evaluation of KIC of brittle

solids by the indentation method with low crack-to-indent ratios. *J Mater Sci Lett* 1982, **1**: 13–16.
[18] Chaim R, Chevallier G, Weibel A, *et al.* Grain growth during spark plasma and flash sintering of ceramic nanoparticles: A review. *J Mater Sci* 2018, **53**: 3087–3105.
[19] Huang JW, Lv XA, Dong XF, *et al.* Synergistic reinforcement of $Si_3N_4$ based ceramics fabricated via multiphase strengthening under low temperature and short holding time. *Materials* 2023, **16**: 6163.
[20] Cao LY, Wang ZH, Yin ZB, *et al.* Investigation on mechanical properties and microstructure of silicon nitride ceramics fabricated by spark plasma sintering. *Mater Sci Eng A* 2018, **731**: 595–602.
[21] Ratzker B, Sokol M, Kalabukhov S, *et al.* High-pressure spark plasma sintering of silicon nitride with LiF additive. *J Eur Ceram Soc* 2018, **38**: 1271–1277.
[22] Ye CC, Jiang Y, Yue XY, *et al.* Effect of temperature and pre-sintering on phase transformation, texture and mechanical properties of silicon nitride ceramics. *Mater Sci Eng A* 2018, **731**: 140–148.
[23] Zheng GM, Zhao J, Li L, *et al.* A fractal analysis of the crack extension paths in a $Si_3N_4$ ceramic tool composite. *Int J Refract Met Hard Mater* 2015, **51**: 160–168.
[24] Wang B, Jiang QG, Liu WY, *et al.* Fabrication of fine-grained α/β $Si_3N_4$ by hot pressing flowing sintering at 1550 ℃. *Ceram Int* 2019, **45**: 13958–13963.
[25] Kumar K, Kim MJ, Oh HM, *et al.* Fabrication of highly dense $Si_3N_4$ via record low-content additive system for low-temperature pressureless sintering. *J Am Ceram Soc* 2022, **105**: 4669–4680.
[26] Belmonte M, Miranzo P, Osendi MI. Mechanical properties and contact damage behavior in aligned silicon nitride materials. *J Am Ceram Soc* 2007, **90**: 1157–1163.
[27] Bódis E, Cora I, Németh P, *et al.* Toughening of silicon nitride ceramics by addition of multilayer graphene. *Ceram Int* 2019, **45**: 4810–4816.
[28] Li PC, Wang T, Guo RP, *et al.* Effect of sintering temperature on hardness gradient of $Si_3N_4$ ceramics fabricated by spark plasma sintering. *Vacuum* 2023, **216**: 112479.
[29] Wu LX, Guo WM, Li JX, *et al.* $Si_3N_4$-$ZrB_2$ ceramics prepared at low temperature with improved mechanical properties. *J Eur Ceram Soc* 2017, **37**: 4217–4221.
[30] Yu JJ, Wei WX, Guo WM, *et al.* Enhanced mechanical properties of $Si_3N_4$ ceramics with $ZrB_2$-B binary additives prepared at low temperature. *J Eur Ceram Soc* 2019, **39**: 5102–5105.
[31] Becher PF. Microstructural design of toughened ceramics. *J Am Ceram Soc* 1991, **74**: 255–269.